Processing and characterization of CoO and Sm_2O_3 codoped ceria solid solution electrolyte

Hong-Chang Yao*, Xue-Li Zhao, Xing Chen, Ji-Chao Wang, Qian-Qing Ge, Jian-She Wang, Zhong-Jun Li

Department of Chemistry, Zhengzhou University, Zhengzhou 450001, PR China

ARTICLE INFO

ABSTRACT

A series of ceria-based solid solution electrolytes, CoO and Sm_2O_3 codoped ceria $Ce_{0.8}Sm_{0.2-x}Co_xO_{2-\delta}$ (denoted as CSO for $x=0$ and CSC_x for $x=0.01–0.09$), are synthesized via a carbonate co-precipitate method. The phase composition of the precursor is determined by XRD, EA and TG/DSC. The oxidation valence of Co in the samples calcined at different temperatures is probed by XPS and determined to be in +2 valence state at the temperature >1000 °C. The sintering investigation demonstrates that the addition of Co promotes densification to occur at lower temperatures with a uniform grain growth. Impedance spectroscopy measurements indicate an improvement in the grain and the grain boundary conductivities for the samples with appropriate Co/Sm ratio. The optimal amount of Co additive is proved to be 7 mol%. It shows that $CSC_{0.07}$ exhibits higher conductivity ($\sigma_t = 0.0538$ S cm^{-1} at 600 °C) and lower activation energy ($E_a = 0.567$ eV) compared with CSO and other CSC_x. The results suggest that cobalt oxide could be used not only as an effective sintering aid but as a favorable dopant to ceria as well.

© 2012 Elsevier B.V. All rights reserved.

1. Introduction

Doped-ceria fluorites have been regarded as potential electrolytes for intermediate temperature solid oxide fuel cells (IT-SOFCs) because of their high ionic conductivity in a low-temperature range (500–700 °C) and their good compatibility with ferritic stainless steels [1–4]. During the past two decades, a number of ceria doped with aliovalent cations, such as rare earth and alkaline earth ions, were synthesized and investigated extensively [5–15]. However, it is well known that being a refractory material, ceria-based ceramics are difficult to be sintered to full density below 1600 °C by conventional solid state technique [16]. Such high sintering temperatures would result in considerable grain coarsening and finally poor mechanical properties. Two measures are thus taken to lower the sintering temperature. The first one is reducing the initial particle size of the powder to the nanometer range by either wet-chemical methods [5,7,8,15] or powder processing techniques [11,17,18], thus increasing the driving force for sintering. Another one is adding small amounts of transition metal oxides as sintering aid to increase the sintering rates. It has been reported that some transition metal oxides, such as MnO_2 [19], Bi_2O_3 [20], CuO [21], MoO_3 [22], Fe_2O_3 [23], and CoO_x [24–32], are very

effective sintering aids for the reduction of the sintering temperature of ceria-based ceramics.

Besides being dense promoters, sintering aids usually exert great influences on the conductivity of the final ceramics. For example, Zhao et al. [20] reported that by using bismuth oxide as sintering aid, the $Sm_{0.2-x}Bi_xCe_{0.8}O_{1.9}$ compacts not only can be densified to nearly theoretical density at 1300 °C but also has much higher ionic conductivity than $Sm_{0.2}Ce_{0.8}O_{1.9}$. Xu et al. [23] reported that the grain-boundary resistance of $Ce_{0.85}Sm_{0.15}O_{1.925}$ could be significantly decreased by small addition of Fe_2O_3. However, the exact roles of transition metal oxides are necessary to study deeply for there are frequently discrepant reports, especially for cobalt oxide as sintering aid. For instance, Pérez-Coll et al. [33] addressed that the addition of cobalt significantly increased the grain boundary conductivity of $Ce_{0.8}Sm_{0.2}O_{2-\delta}$ ceramics, while Zhang et al. [34] suggested that the addition of cobalt in $Ce_{0.8}Gd_{0.2}O_{2-\delta}$ samples show a slight effect on the grain boundary conductivity. Some authors [28,29], however, pointed out that the addition of Co greatly improved both grain boundary and bulk conductivity. On the other hand, the solubility of cobalt oxide in doped-ceria ceramics reported in the literatures differed considerably. Sirman et al. [35] reported the solubility limit of CoO in CGO was less than 0.5 mol% at 1400 °C, while Kharton et al. [36] pointed out that the solubility limit of cobalt oxide in CGO20 was up to 10–15 mol%. Apart from the solubility, another puzzled problem is the oxidation state of Co in the ceramics because the reporting existence included CoO, Co_3O_4 and Co_2O_3 [24–32]. In the light of the above inconsistency, it is thus necessary to

further determine the exact manner of Co additive in the doped-ceria ceramic.

As an intensively investigated sintering aid, the introduction of cobalt was mainly concentrated on commercially available powders coated with cobalt nitrate [24–28]. Few papers focused on optimizing the homogenization of cations [31]. In this study, different compositions of $Ce_{0.8}Sm_{0.2-x}Co_xO_{2-\delta}$ with varying Co/Sm ratio (abbreviated as CSO for $x = 0$ and CSC_x for $x = 0.01$–0.09) have been prepared via co-precipitation method. The valence state of Ce and Co was determined by XPS. The densification of the compacts was investigated and special attention was paid to the location and solubility of Co. The influences of Co additive on the bulk and grain boundary conductivity were studied and discussed. Interesting, the addition of Co in the $Ce_{0.8}Sm_{0.2-x}Co_xO_{2-\delta}$ series results in not only a relatively homogeneous microstructure but also a remarkably improved in both the grain and grain boundary conductivities. In comparison with most metal oxides acting merely as sintering acids [19–23], the report provides more information on the effect of CoO-addition on the electrical properties.

2. Experimental

2.1. Sample preparation

Powders of composition CSC_x ($x = 0.01$–0.09) were prepared by oxalate co-precipitation method using cerium nitrate, samarium nitrate and cobalt nitrate as starting materials. The appropriate quantities of starting materials were dissolved in water, mixed and co-precipitated with ammonium oxalate solution. Sm-doped ceria without Co addition was also prepared under the same experimental conditions, for comparison purpose. The as-synthesized powders were dried at 60 °C in an oven and subsequently calcined at 600 °C for 4 h to decompose the carbonates and to favor the formation of the fluorite phase. After calcination, the doped powders were uniaxially pressed (10 MPa) into cylindrical pellets of 13 mm in diameter in a steel die followed by isostatic pressing (180 MPa). The shaped samples were sintered at different constant temperatures from 1200 to 1400 °C for 4 h in air at a heating rate of 8 °C min^{-1} below 1000 °C and 3 °C min^{-1} above 1000 °C. The apparent densities of sintered pellets were determined by Archimedes principle using water as immersing medium.

2.2. Property measurements

Powder X-ray diffraction (XRD) intensities were recorded with X-ray diffractometer (PANalytical X'Pert PRO, Netherlands) operating with Ni β-filtered at 40 kV and 40 mA, using CuKα radiation ($\lambda_{K\alpha 1} = 1.540598$ Å, $\lambda_{K\alpha 2} = 1.544426$ Å). The crystalline phases were analyzed with PANalytical X'Pert High Score Plus program and identified using the International Centre for Diffraction Data (ICDD) Powder Diffraction Files (PDF). Lattice parameters were calculated by Rietveld method. Thermal decomposition of the precursors was monitored by Thermogravimetric and Differential Scanning Calorimeter (TG/DSC) with instrument NETZSCH STA 409 PC/PG in flowing air with heating rate of 10 °C min^{-1} in alumina crucible up to 1000 °C. The elemental analysis (EA) was performed with a Flash EA 1112 elemental analyzer.

X-ray photoelectron spectroscopy (XPS) measurements were carried out at room temperature on a Perkin Elmer PHI 5300 X-ray Photoelectron Spectrometer. Al K$_\alpha$ radiation ($h\nu = 1486.6$ eV) was adopted as the excitation source, operating at 250 W with 12.5 kV acceleration voltage. The pass energy of the survey scan was 89.45 eV and that of detail scan was 35.75 eV with a resolution of 1 and 0.2 eV, respectively. Before being sent to the chamber, each sample was cleaned carefully. The base pressure of the
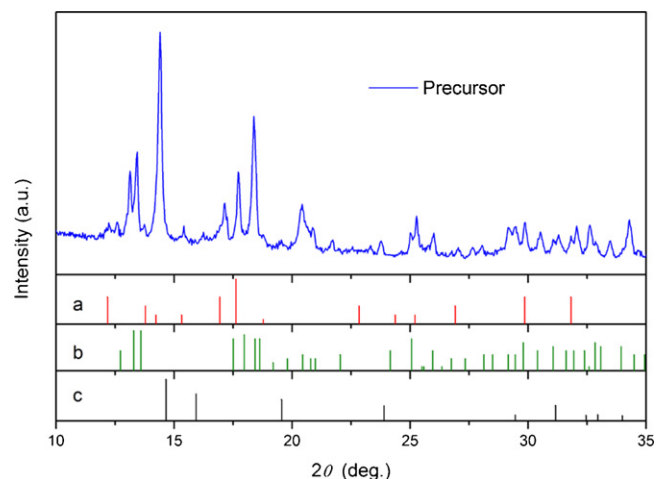

Fig. 1. XRD patterns of the as-dried oxalate co-precipitate and the referenced PDF index species: (a) $Ce(NH_4)(C_2O_4)_2 \cdot H_2O$, (b) $Sm_2(C_2O_4)_3 \cdot 10H_2O$ and (c) $CoC_2O_4 \cdot 4H_2O$.

instrument was 9.5×10^{-8} torr (1 torr = 133.3 Pa). Binding energy was calibrated referenced to the C 1s peak (284.6 eV).

The microstructures of the sintered pellets were observed using a scanning electron microscope (JEOL JSM–6700 FE–SEM) in polished and thermally etched pellets at the temperature below 100 °C of the sintering temperature during 30 min. INCA X-ray microanalysis system (OXFORD) was used to detect energy dispersive spectroscopy (EDS) for elemental analysis in micro-regions of sintered pellets.

2.3. Electrical measurements

The ionic conductivity measurements were performed by an ac (alternating current) complex impedance method at frequencies range from 0.1 Hz to 1 MHz on a PARSTAT 2273 impedance analyzer. Before measurements, silver paste was painted on two sides of the disk as electrodes, and the disk was then dried and fired at 800 °C for 30 min to erase the solvent. The measurements were conducted in air in the temperature range from 250 to 650 °C with an increment of 50 °C. Bulk and grain boundary ionic conductivity were measured using an impedance spectroscopy. Curve fitting and resistance calculation were done by ZSimpWin software. The conductivities were calculated using the expression of $\sigma = l/SR$, where l is the sample thickness and S is the electrode area of the sample surface. Activation energies (E_a) were calculated by fitting the conductivity data to the Arrhenius relation for thermally activated conduction, which is given as $\sigma T = \sigma_0 \exp(-E_a/kT)$, where $\sigma, \sigma_0, E_a, k, T$ are the conductivity, pre-exponential factor, activation energy, Boltzmann constant and absolute temperature, respectively.

3. Results and discussion

3.1. Powder synthesis and characterization

The representative XRD pattern of the precursor of nominal composition $CSC_{0.05}$ was measured and the compositions were identified to be composed of $Ce(NH_4)(C_2O_4)_2 \cdot H_2O$ (PDF No. 00-019-0277), $Sm_2(C_2O_4)_3 \cdot 10H_2O$ (PDF No. 00-020-1021), $CoC_2O_4 \cdot 4H_2O$ (PDF No. 00-037-0534) (Fig. 1). To further determine the ingredient, EA was performed and the results showed that the precursor contained 12.64 wt% of C, 2.17 wt% of H and 3.02 wt% of N. The TG/DSC of the precursor was also investigated and the results are shown in Fig. 2. As can be seen, the decomposition of the precursor proceeds through two distinct stages. The first one with a weight loss
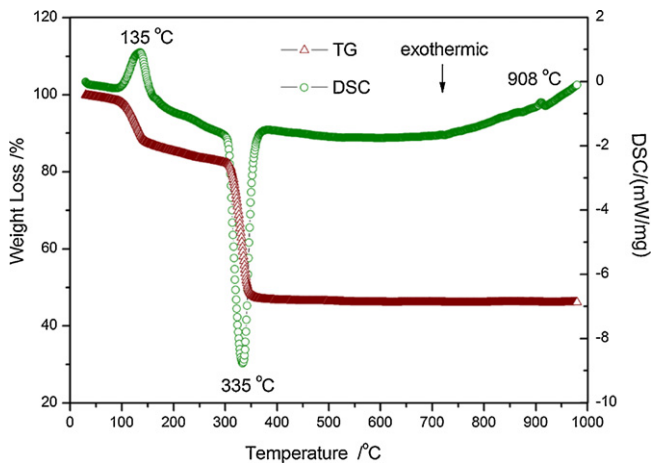
Fig. 2. TG/DSC curves of the precursor conducted at a heating rate of $10\,°C\,min^{-1}$ from room temperature to $1000\,°C$ in air.

Fig. 4. XPS spectra of Co 2p from surface region of $Ce_{0.8}Sm_{0.13}Co_{0.07}O_{2-\delta}$ sintered at (a) $600\,°C$ and (b) $1000\,°C$.

of 13.1%, accompanied by a strong endothermic peak at $135\,°C$, may be attributed to the evaporation of the absorbed moisture and the release of ammonia and water. The second stage with a weight loss of 39.6%, accompanied by an exothermic peak at $335\,°C$, may correspond to the decomposition of the oxalate. It is noteworthy that there is a small endothermic peak at $908\,°C$, which may be due to the transformation of Co_3O_4 to CoO [37].

Based upon the above results and considering molecular electrical neutrality, the precursor is assumed to be $Ce_{0.8}Sm_{0.15}Co_{0.05}(NH_4)_{0.8}(C_2O_4)_{1.875}\cdot1.75H_2O$. The final weight loss (52.4%) is in good agreement with that calculated (51.9%) from the composition to $CSC_{0.05}$.

XPS analysis was carried out to characterize the valence state of Ce and Co ions. Fig. 3 shows the XPS results of the $CSC_{0.07}$ samples sintered at different temperature. According to the published results, six peaks labeled as v_0, v_1, v_2, v'_0, v'_1 and v'_2 at different bonding energy are attributed to the feature peaks of Ce^{4+} 3d [38,39]. However, typical peaks at u_1 and u'_1, characteristic of Ce^{3+}, are not observed. Besides, the attenuation of v'_2 peak or the increase of doublet u_1/u'_1 is not observed, which is often used to approximate the level of surface reduction [38]. Therefore, it becomes evident that Ce is in the tetravalent state in the samples sintered at different temperatures.
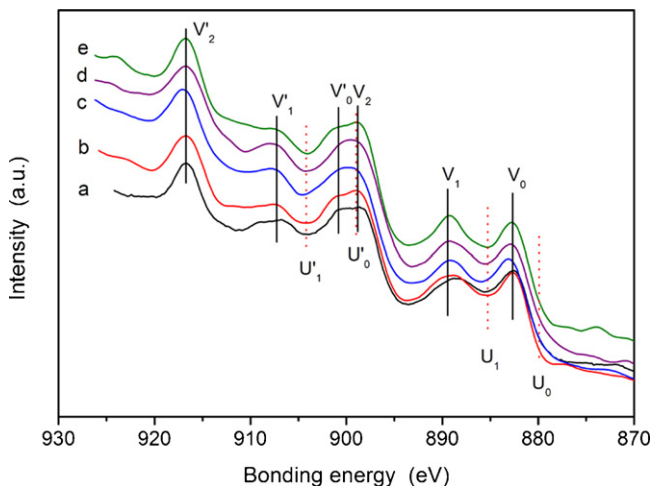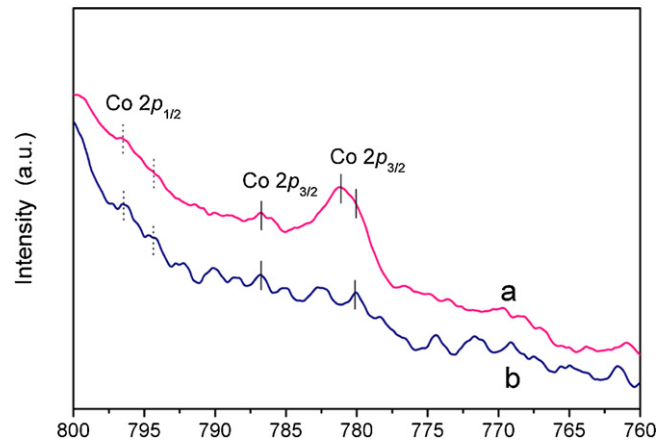
The Co 2p XPS spectra of $CSC_{0.07}$ sintered at different temperatures were surveyed. However, no distinct peaks of Co2p signals were detected for those sintered at $1200–1400\,°C$, probably due to solid dissolution of cobalt inside CeO_2, except the sample sintered at $600\,°C$ and $1000\,°C$ (Fig. 4). As it can be seen from Fig. 4a that peaks at 781.1 eV and 786.8 eV binding energy and peak at 796.0 eV binding energy were appeared, which is corresponding to the Co 2$p_{3/2}$ and Co 2$p_{1/2}$ structure of Co 2p, respectively. According to Carson et al. [40], the Co 2p XPS peak positions agree with the presence of Co_3O_4. However, the peak intensity changed greatly when the calcination temperature increased up to $1000\,°C$. Comparing the peak intensity with that of sample sintered at $600\,°C$, the degradation of the peak at 781.1 eV means the reduction of Co_3O_4 content and the enhancement of the ratio of CoO, according to Carson et al. [40]. CoO is thus believed to be the existence in the crystalline at high temperatures. Considering the transformation temperature of Co_3O_4 to CoO [37], it is believable to identify cobalt as Co^{2+} though some authors regarded cobalt as Co^{3+} [26].

As the investigated samples have more than one cation, it is difficult to assign the oxygen peaks. A multi-peaks Gaussian fitting was thus used to interpret the spectra of $CSC_{0.07}$ sample sintered at $600\,°C$ and the results showed O 1s spectra with three distinct peaks (Fig. 5). The most intense peak at 528.6 eV may be assigned to the lattice oxygen of $CSC_{0.07}$ [41] while the peak at 530.2 eV may be attributed to cobalt oxide [42]. The shoulder peak at 532.0 eV
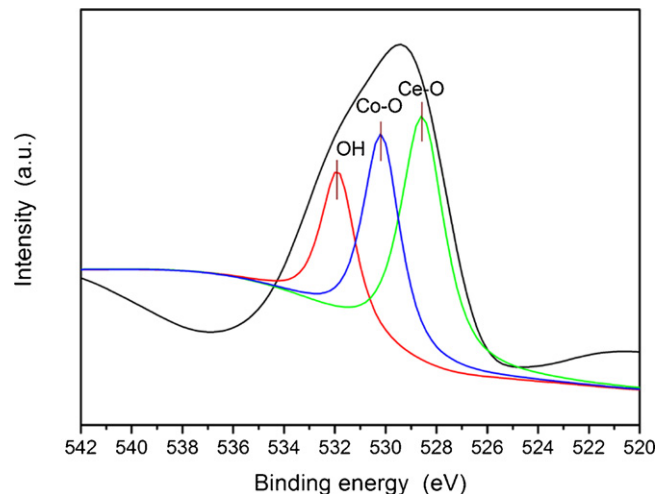

Fig. 3. Ce 3d XPS spectra of the $Ce_{0.8}Sm_{0.13}Co_{0.07}O_{2-\delta}$ samples sintered at (a) $600\,°C$; (b) $1000\,°C$; (c) $1200\,°C$; (d) $1300\,°C$ and (e) $1400\,°C$.

Fig. 5. XPS spectra of O 1s from surface region of $Ce_{0.8}Sm_{0.13}Co_{0.07}O_{2-\delta}$ sintered at $600\,°C$.
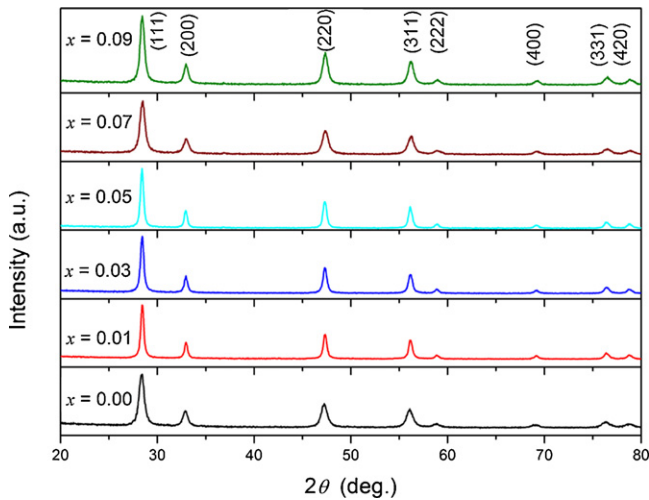
Fig. 6. XRD patterns of the $Ce_{0.8}Sm_{0.2-x}Co_xO_{2-\delta}$ calcined at 600 °C.

Fig. 8. Sintered density as a function of cobalt content.

is assigned to some hydroxyl like groups, which presumably result from surface bonded water [43].

Fig. 6 illustrates the XRD patterns of the calcined powders of CSC_x at different dopant contents. The diffraction peaks were indexed to (1 1 1), (2 0 0), (2 2 0), (3 1 1), (2 2 2), (4 0 0), (3 3 1) and (4 2 0) planes, matching well those of the face-centered cubic fluorite structure of CeO_2 (PDF No. 00-34-0394). It can be seen that no evident secondary phases (CoO or Co_3O_4) could be identified. Rietveld refinement was thus applied to the diffraction patterns and the results are listed in Table 1. The lattice parameters as a function of cobalt are plotted in Fig. 7. With Co content increasing, the lattice parameter decreases linearly as $a(x) = 5.4310 - 0.0796x$ and the R^2 value is 0.9841 for CSC_x ($x = 0.01$–0.09) powders. Cobalt ions are accordingly regarded as incorporating into the ceria structure to form solid solution. The result accords well with the Vegard's Slope quality factor which may be identified beneficial sintering aids in ceria electrolytes [44]. Also, the result is in good agreement with that reported by Kharton et al. [36].

When CoO is dissolved in the lattice, the reaction (using Kroeger–Vink notation) can be expressed as:

$$CoO \xrightarrow{CeO_2} Co''_{Ce} + O_O^\times + V_O^{\cdot\cdot} \tag{1}$$

The formation of the positive charged vacancy may induce the increase of the bulk conductivity of CSC_x as shown below.
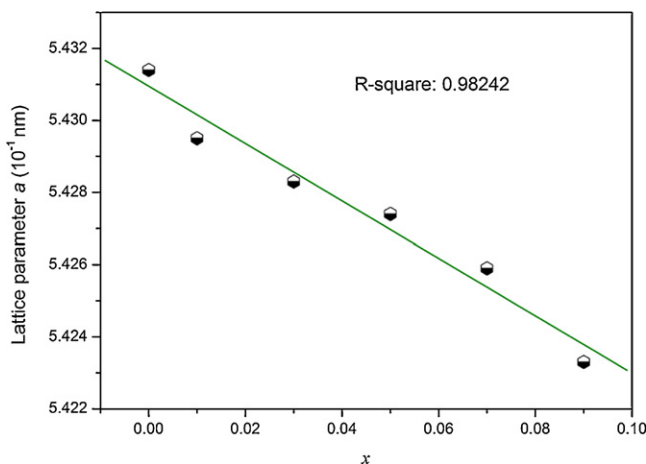

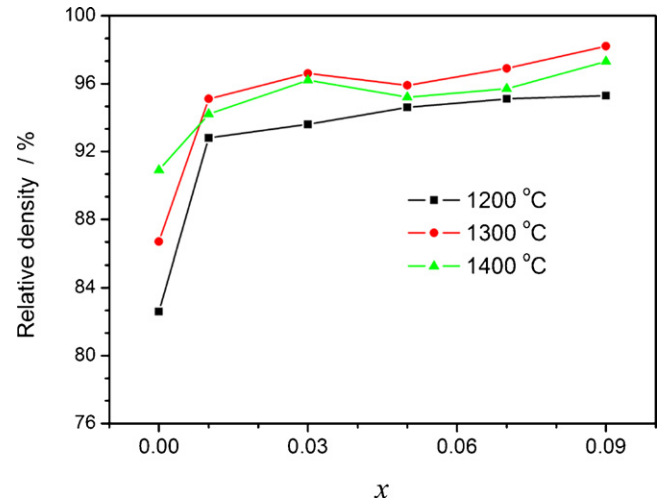**Fig. 7.** Lattice constant of $Ce_{0.8}Sm_{0.2-x}Co_xO_{2-\delta}$ powders as a function of x.

3.2. Sintering

Fig. 8 shows the effect of Co additive on the densification of CSC_x samples heat-treated at 1200–1400 °C. The beneficial effect of Co additive on the relative density is obvious and found that minor, 1 mol%, additions of cobalt sintering aids can produce enhancements of relative density up to 92.8% after sintered at 1200 °C, while the Co-free composition, CSO, reached only 90.9% after sintered at 1400 °C. A reduction in sintering temperature of ~200 °C for CSC_x was achieved compared with CSO. It is worth noting that when the temperature reached 1400 °C, visible decreases in relative densities are observed, which may be related to the change of the microstructure due to high temperature.

The microstructures of the sintered pellets were investigated and the typical SEM images of CSO and CSC_x ($x = 0.07$ or 0.09) pellets sintered at different temperatures are shown in Fig. 9. The CSO sample sintered at 1200 °C is very porous (with only 82.6% relative density) and the pores are found to be continuous and open (Fig. 9a). But, in contrast, the $CSC_{0.07}$ pellet at 1200 °C is well sintered with few closed pores and grains connect to each other, which are in accordance with the density measurements (Figs. 9b and 8). With increasing the temperature, the grain size of $CSC_{0.07}$ pellet increases from 0.5 μm to 1–3 μm (Fig. 9c and d). From the distinct and clean grain boundaries in images of Fig. 9c, we can conclude that Co additive distributes uniformly in the sample. However, new segregation phase seems to be formed at the grain boundaries of $CSC_{0.07}$ when the temperature reaches to 1400 °C (Fig. 9d). Such a location was analyzed by EDS coupled to scanning electron microscope. Fig. 9f shows EDS spectra of the sintered pellets and results of the elemental analysis, which is averaged values over four independent determinations. The calculated values of element analysis prove that the segregation phase is mainly CoO, which is in good agreement with the results of XPS data. Similar to $CSC_{0.07}$ sintered at 1400 °C, CoO phase is also found at the grain boundary region of $CSC_{0.09}$ pellet sintered at 1300 °C (Fig. 9e). The emergence of CoO phase for $CSC_{0.09}$ sintered at 1300 °C and for $CSC_{0.07}$ sintered at 1400 °C was also confirmed by XRD measurements (not shown). Therefore, the optimal concentration of Co in CSO was determined to be around 7% and the optimal sintering temperature was selected to 1300 °C.

3.3. Electrical conductivity

The electrical conductivities of $CSCo_x$ sintered at 1300 °C were studied by ac impedance spectroscopy. Figs. 10 and 11 show the
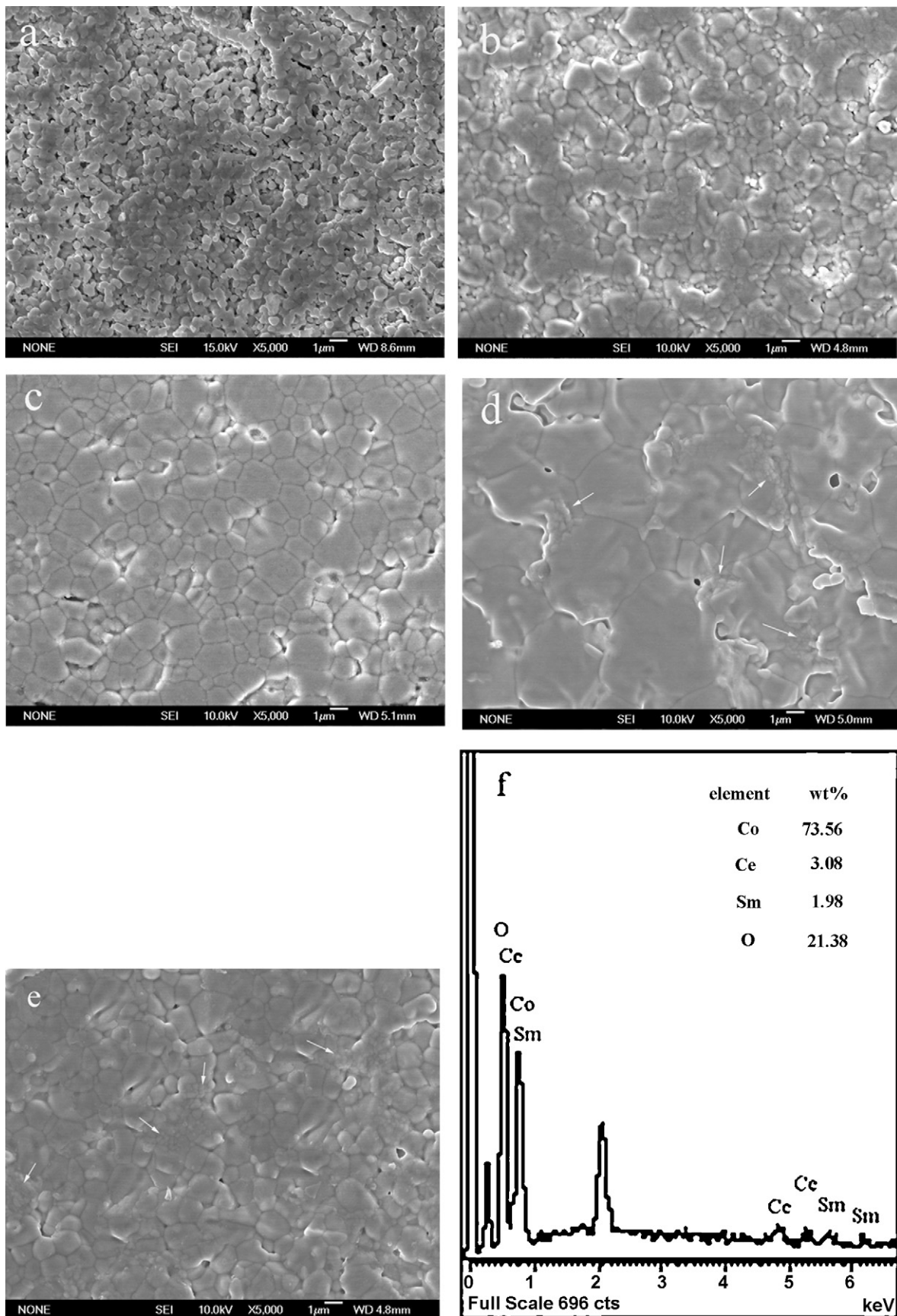
Fig. 9. SEM images of thermally etched surfaces of (a) CSO sintered at 1200 °C for 4 h; (b) CSOCo$_{0.07}$ sintered at 1200 °C for 4 h; (c) CSOCo$_{0.07}$ sintered at 1300 °C for 4 h; (d) CSOCo$_{0.07}$ sintered at 1400 °C for 4 h; and (e) CSOCo$_{0.09}$ sintered at 1300 °C for 4 h.

Table 1
Refined unit cell values, Rietveld disagreement factors and calculated properties of the $Ce_{0.8}Sm_{0.2-x}Co_xO_{2-\delta}$ ($x = 0.00$–0.09) series.

Parameters	Samples					
	CSO	CSC$_{0.01}$	CSC$_{0.03}$	CSC$_{0.05}$	CSC$_{0.07}$	CSC$_{0.09}$
a (Å)	5.4314	5.4295	5.4283	5.4274	5.4259	5.4233
V (Å^3)	160.2	160.06	159.95	159.87	159.74	159.51
R_e	6.76	6.52	6.27	6.66	6.22	6.57
R_p	5.64	6.18	5.92	6.03	4.89	5.91
R_{wp}	7.32	7.93	7.71	7.76	6.46	7.66
GOF	1.18	1.65	1.53	1.36	1.08	1.36
Expected oxygen vacancy	0.10	0.105	0.115	0.125	0.135	0.145
FV ratio [%][a]	40.6	41.0	41.8	42.7	43.5	44.3

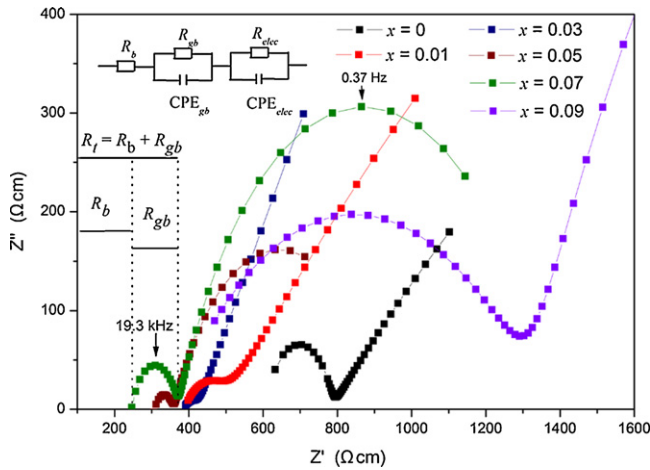[a] FV ratio [%] = $\{a^3 - 4 \times (4\pi/3) \times (r_{c,avg}^3 + 2r_o^3)]\}/a^3$ (from Ref. [50]).

Fig. 10. Impedance spectra and equivalent circuit of $Ce_{0.8}Sm_{0.2-x}Co_xO_{2-\delta}$ sintered at 1300 °C for 4 h at a measurement temperature of 350 °C in air.

typical impedance spectra for the CSO and CSC$_x$ ($x = 0.01$–0.09) pellets measured at 350° and 600 °C. It can be seen that at 350 °C there exists a depressed semicircle and an arc for different samples, which correspond to grain boundary resistance and electrode polarization, respectively. With increasing the temperature to 600 °C, only one arc remains while the depressed semicircle is replaced by a large "tail" which may be attributed to the inductance of the experiment setup [45]. From Figs. 10 and 11, it can also find the evolution of the impedance arcs as a function of the CoO concentration. Similar results were found in gadolinia-doped
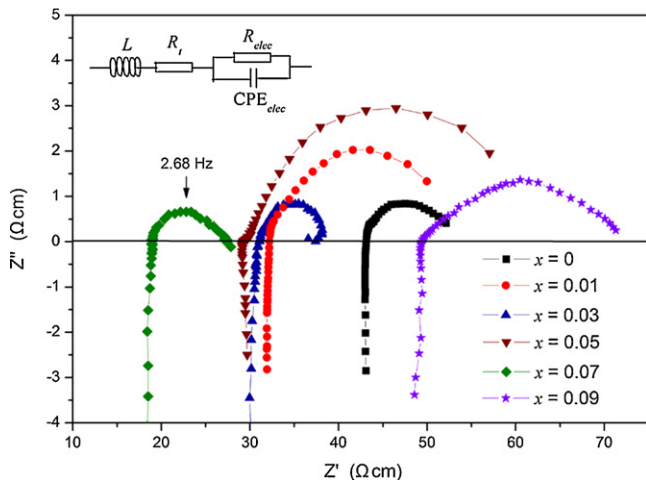
ceria with bismuth oxide as sintering aid [46]. In contrast with the sample $Ce_{0.9}Sm_{0.1}O_{1.95}$ with 0.5% Co addition synthesized by conventional mixed oxide method [29], the grain boundary resistance in Fig. 10 is obviously small. This indicates that the co-precipitation method is favorable for Co distribution in CSO, and for improving the electrical properties of the samples.

The conductivities can be calculated using the resistance obtained by fitting the impedance spectra with equivalent circuit models (inset in Figs. 10 and 11) using ZSimpWin software. In Figs. 10 and 11, R_b, R_{gb}, R_{elec}, L, CPE$_{gb}$ and CPE$_{elec}$ stand for bulk resistance, grain boundary resistance, electrode resistance, inductance of the experiment setup, CPE of grain boundary and CPE of electrode, respectively. The total resistance of electrolyte is given by $R_t = R_b + R_{gb}$. Then the conductivity datum σ_i at different temperatures can be obtained using the equation $\sigma_i = l/SR_i$ (i = b, gb or t).

Fig. 12 shows the calculated total conductivity as a function of temperature following Arrhenius equation $\sigma T = \sigma_0 \exp(-E_a/kT)$. Table 2 presents a summary of the representative conductivity data. It can be observed that the conductivities of CSC$_x$ ($x = 0.01$–0.07) are higher than that of CSO, while the conductivity of CSC$_{0.09}$ is lower than that of CSO. As shown in Table 2, the electrical conductivity of CSC$_{0.07}$ can reach as high as 0.0229 S cm^{-1} at 500 °C and 0.0538 S cm^{-1} at 600 °C, which are among the highest values observed in electrolytes considered as candidates for IT-SOFCs. The conductivity of CSC$_{0.07}$ at 600 °C can be compared with that of $Ce_{0.8}Sm_{0.05}Ca_{0.15}O_{2-\delta}$ electrolyte ($\sigma_t = 0.052$ S cm^{-1} at 600 °C) [47]. And it is much higher than that of $Ce_{0.79}Gd_{0.20}Co_{0.01}O_{2-\delta}$ ($\sigma_t = 0.021$ S cm^{-1} at 600 °C) [31] as well as 1CoGDC10 [48] and 1CoGDC20 [25].

Fig. 11. Impedance spectra and equivalent circuit of $Ce_{0.8}Sm_{0.2-x}Co_xO_{2-\delta}$ sintered at 1300 °C for 4 h at a measurement temperature of 600 °C in air.
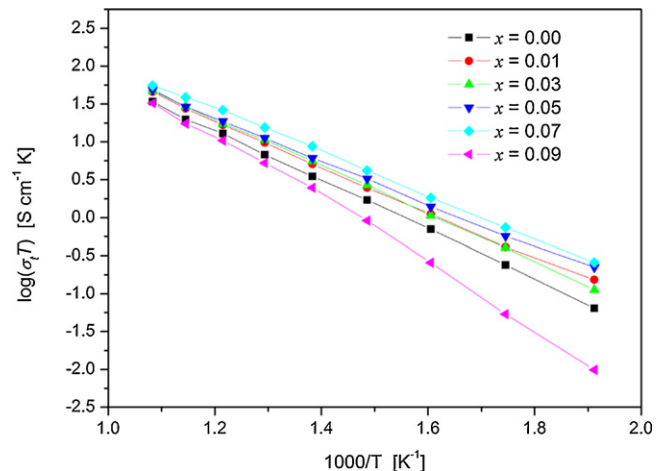

Fig. 12. Arrhenius plots for the total conductivities of $Ce_{0.8}Sm_{0.2-x}Co_xO_{2-\delta}$ electrolytes sintered at 1300 °C for 4 h.

Table 2
Total conductivity and activation energy for $Ce_{0.8}Sm_{0.2-x}Co_xO_{2-\delta}$ electrolytes sintered at 1300 °C.

Samples	Electrical conductivity $\sigma_t (\times 10^{-2}\,S\,cm^{-1})$				$E_{a,b}$ (eV) 250–650 °C	$E_{a,gb}$ (eV) 250–450 °C	$E_{a,t}$ (eV) 250–650 °C
	500 °C	550 °C	600 °C	650 °C			
CSO	0.87	1.56	2.27	3.68	0.58	0.94	0.645
$CSC_{0.01}$	1.27	2.03	3.16	4.98	0.56	0.93	0.624
$CSC_{0.03}$	1.46	2.12	3.36	5.08	0.55	0.98	0.596
$CSC_{0.05}$	1.49	2.27	3.32	5.29	0.54	0.72	0.561
$CSC_{0.07}$	2.29	3.66	5.38	7.88	0.52	1.01	0.567
$CSC_{0.09}$	1.04	1.58	2.08	3.51	0.58	1.08	0.845

The bulk conductivity of the studied samples as a function of temperature is shown in Fig. 13. As can be seen, with increasing Co content, the bulk conductivities increase with Co concentration and maximum values are reached for the sample $CSOCo_{0.07}$. When analyzing the bulk conductivity, one should take into account the migration enthalpy (ΔH_m) for oxide anions through the ceria lattice. According to Zhao et al. [20], ΔH_m is the sum of the energy required to break a lattice cation–oxygen bond and an energy term related to the free volume. The average M—O binding energy (ABE), which is defined as $ABE = (1-x)\,BE\,(Ce—O) + x\,BE\,(Sm/Co—O)$, decreases linearly with increasing Co content due to the weaker Co—O bond dissociation enthalpy [49]. The free volume ratios, which were calculated from the effective ionic radii [50], increase with increasing Co substitution (see Table 1). More importantly, the concentration of oxygen vacancy increases due to Co substitution (Eq. (1)). Thus, the bulk conductivities increase with increasing Co content. However, at higher Co substitution, the bulk conductivities decrease, probably due to the increasing contribution of the defect association [1] and/or due to the presence of a second phase (Fig. 9e). This result differs from that of Kleinlogel and Gauckler [25], i.e. σ_b remained unchanges compared to pure CGO when CGO doping Co. However, similar results had also been reported by Lewis et al. [26], who claimed that for 2CoCGO, σ_b was enhanced due to the increase of additional oxygen vacancies.

Arrhenius plots of the grain boundary conductivity of the studied samples are displayed in Fig. 14. It shows that the grain boundary conductivity increases and attains a maximum at 5 mol%. Out of this range, the conductivity reduces rapidly as increasing Co content. This may be firstly explained by the fact that cobalt is very prone to segregate at grain boundaries due to the weaker Co—O bond dissociation enthalpy (368 kJ mol⁻¹) than Ce—O (795 kJ mol⁻¹) and Sm—O (619 kJ mol⁻¹) [49], thus preventing

segregation of other additives. On the other hand, the transfer of Co to the grain boundaries will construct space–charge layers, which had been proved to be favorable to improvement of the grain boundary conductivity of $Ce_{0.8}Ln_{0.2}O_{2-\delta}$ with Co-doping [33,51]. In addition, as Co^{2+} is smaller than Ce^{4+}, it can enhance grain boundary mobility due to the large distortion of the surrounding lattice that facilitates defect migration of ceria [30]. Grain boundary conductivity was thus improved. With the accumulation of Co at grain boundaries, however, the space-charge layers become more and more thick, blocking oxygen vacancies across the grain boundaries and finally resulting in the decrease of σ_{gb}. Even worse is the secondary phase separating from the main phase, which directly results in the rapid decrease of σ_{gb}. Therefore, the optimal dopant concentration of Co is assumed to be 5–7 mol% considering the effects of Co concentration on σ_b and σ_{gb}.

The activation energies calculated from Figs. 12–14 are presented in Table 2. The activation energies, $E_{a,b}$, in the entire explored region are found to be very close (0.52–0.58 eV), which indicates the similar conduction mechanism among the samples with different Co/Sm ratio. The values of $E_{a,gb}$, however, is very different, which means different conduction mechanism as stated above. From Figs. 10–14 and Table 2, we can also find that the relative contribution of the grain interior and grain boundaries to the total conductivities. For any sample, the grain boundary effect becomes smaller with increasing temperature. And at any particular temperature, the contribution from the grain boundaries first increases and then decreases with the increase of cobalt content. Therefore, the grain boundary process dominates the conduction process. As far as the effect of Co is concerned, both the grain and grain boundary conductivity can be greatly influenced by the addition of Co. The conclusion is in accordance with that drawn from Pérez-Coll et al. [28] and Ayawanna et al. [29].
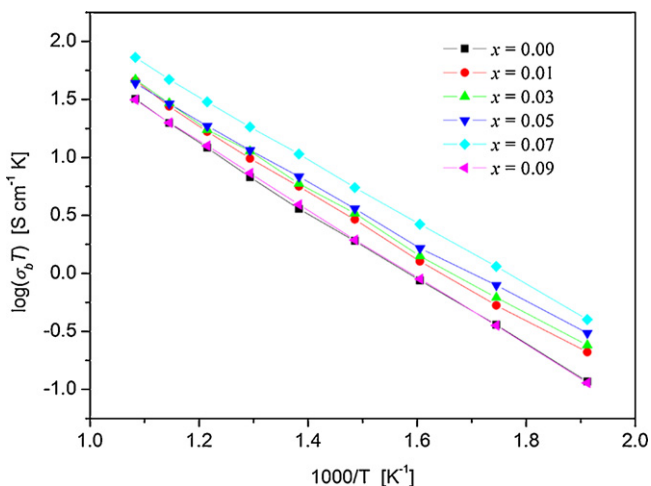

Fig. 13. Arrhenius plots for the grain conductivities of $Ce_{0.8}Sm_{0.2-x}Co_xO_{2-\delta}$ electrolytes sintered at 1300 °C for 4 h.

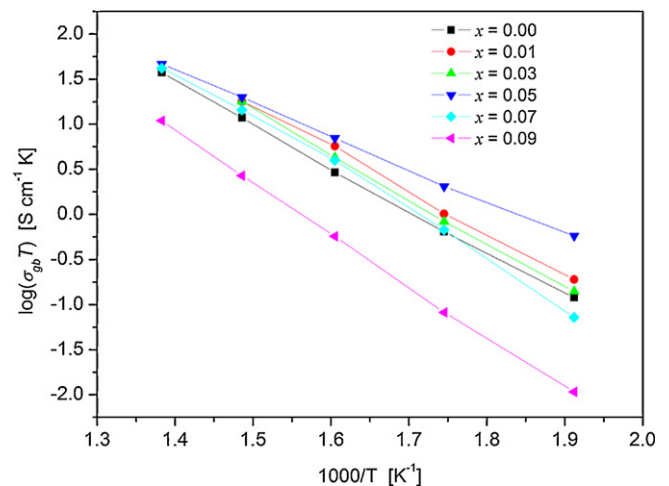**Fig. 14.** Arrhenius plots for the grain boundary conductivities of $Ce_{0.8}Sm_{0.2-x}Co_xO_{2-\delta}$ electrolytes sintered at 1300 °C for 4 h.

For an electrolyte operating at intermediate temperatures, it should possess as high lattice conductivity and grain boundary conductivity as possible. The as-synthesized CSC$_{0.05}$ and CSC$_{0.07}$, with high σ_b and σ_{gb}, is thus a promising electrolyte for IT-SOFCs. However, their stability at operating temperatures is necessary to further examine. And this work is under way in our laboratory.

4. Conclusions

This work has investigated powder characteristics and sintering of CSO and CSC$_x$ electrolyte powders made by carbonate co-precipitate method. Density measurements suggested that a reduction of about 200 °C in densification sintering temperature of CSC$_x$ was obtained when compared with CSO. Much attention has been paid to the solubility, location and oxidation state of Co in the sintered ceramics. The results show that CoO is the main species in the sintered ceramics with cobalt distributing homogeneously in the lattice under the condition of Co content less than 7 mol% and sintering temperature lower than 1300 °C. Of special interest in this work is the relative contribution of Co addition to the grain and grain boundary conductivities. The results showed that co-doping with appropriate Co/Sm ratio led to an improvement of both the bulk and the grain boundary conductivities. The highest total conductivity for CSOCo$_{0.07}$ at 600 °C was 0.0538 S cm^{-1}, which could be compared with that of well-known Ce$_{0.8}$Sm$_{0.2-x}$Ca$_x$O$_{1.9}$ system. It suggested that cobalt oxide could be served not only as an effective densification promoter but also as a favorable dopant to ceria-based electrolytes.

Acknowledgments

References

[1] H. Inaba, H. Tagawa, Solid State Ionics 83 (1996) 1.
[2] M. Mogensen, N.M. Sammes, G.A. Tompsett, Solid State Ionics 129 (2000) 63.
[3] V.V. Kharton, F.M.B. Marques, A. Atkinson, Solid State Ionics 174 (2004) 135.
[4] D.J.L. Brett, A. Atkinson, N.P. Brandon, S.J. Skinner, Chem. Soc. Rev. 37 (2008) 1568.
[5] W. Huang, P. Shuk, M. Greenblatt, Chem. Mater. 9 (1997) 2240.
[6] S. Zha, C. Xia, G. Meng, J. Power Sources 115 (2003) 44.
[7] H. Xu, H. Yan, Z. Chen, J. Power Sources 163 (2006) 409.
[8] V. Thangadurai, P. Kopp, J. Power Sources 168 (2007) 178.
[9] S. Kuharuangrong, J. Power Sources 171 (2007) 506.
[10] V. Espositow, E. Traversa, J. Am. Ceram. Soc. 91 (2008) 1037.
[11] M.G. Bellino, D.G. Lamas, N.E.W. de Reca, Adv. Funct. Mater. 16 (2006) 107.
[12] C. Laberty-Robert, J.W. Long, K.A. Pettigrew, R.M. Stroud, D.R. Rolison, Adv. Mater. 19 (2007) 1734.
[13] H. Li, C. Xia, M. Zhu, Z. Zhou, G. Meng, Acta Mater. 54 (2006) 721.
[14] D.R. Ou, T. Mori, F. Ye, M. Takahashi, J. Zou, J. Drennan, Acta Mater. 54 (2006) 3737.
[15] R.O. Fuentes, R.T. Baker, J. Power Sources 186 (2009) 268.
[16] Z. Zhan, T.-L. Wen, H. Tu, Z.-Y. Lu, J. Electrochem. Soc. 148 (2001) A427.
[17] T.S. Zhang, J. Ma, L.B. Kong, P. Hing, Y.J. Leng, S.H. Chan, J.A. Kilner, J. Power Sources 124 (2003) 26.
[18] T. Mori, T. Kobayashi, Y. Wang, J. Drennan, T. Nishimura, J.-G. Li, H. Kobayashi, J. Am. Ceram. Soc. 88 (2005) 1981.
[19] T. Zhang, P. Hing, H. Huang, J. Kilner, Mater. Lett. 57 (2002) 507.
[20] W. Zhao, S. An, M. Liang, J. Am. Ceram. Soc. 94 (2011) 1496.
[21] Y. Dong, S. Hampshire, B. Lin, Y. Ling, X. Zhang, J. Power Sources 195 (2010) 6510.
[22] G. Zhao, D. Zhou, J. Zhu, M. Yang, J. Meng, Solid State Sci. 13 (2011) 1072.
[23] D. Xu, X. Liu, S. Xu, D. Yan, L. Pei, C. Zhu, D. Wang, W. Su, Solid State Ionics 192 (1999) 510.
[24] C. Kleinlogel, L.J. Gauckler, Adv. Mater. 18 (2001) 1081.
[25] C. Kleinlogel, L.J. Gauckler, Solid State Ionics 135 (2000) 567.
[26] G.S. Lewis, A. Atkinson, B.C.H. Steele, J. Drennan, Solid State Ionics 152–153 (2002) 567.
[27] D.P. Fagg, J.C.C. Abrantes, D. Peŕez-Coll, P. Núñez, V.V. Kharton, J.R. Frade, Electrochim. Acta 48 (2003) 1023.
[28] D. Pérez-Coll, P. Núñez, J.C.C. Abrantes, D.P. Fagg, V.V. Kharton, J.R. Frade, Solid State Ionics 176 (2005) 2799.
[29] J. Ayawanna, D. Wattanasiriwech, S. Wattanasiriwech, P. Aungkavattana, Solid State Ionics 180 (2009) 1388.
[30] H. Yoshida, T. Inagaki, J. Alloys Compd. 408–412 (2006) 632.
[31] A. Dutta, A. Kumar, R.N. Basu, Electrochem. Commun. 11 (2009) 699.
[32] D. Peŕez-Coll, P. Núñez, J.C. Ruiz-Morales, J. Peña-Martínez, J.R. Frade, Electrochim. Acta 52 (2007) 2001.
[33] D. Pérez-Coll, D. Marrero-López, P. Núñez, S. Piñol, J.R. Frade, Electrochim. Acta 51 (2006) 6463.
[34] T.S. Zhang, J. Ma, Y.J. Leng, S.H. Chan, P. Hing, J.A. Kilner, Solid State Ionics 168 (2004) 187.
[35] J.D. Sirman, D. Waller, J.A. Kilner, in: U. Stimming, S.C. Singhal, H. Tagawa, W. Lehnert (Eds.), Proceedings of the Fifth International Symposium on Solid Oxide Fuel Cells (SOFC-V), Aachen, Germany, 1997, pp. 1159–1167.
[36] V.V. Kharton, F.M. Figueiredo, L. Navarro, E.N. Naumovich, A.V. Kovalevsky, A.A. Yaremechenko, A.P. Viskup, A. Carneiro, F.M.B. Marques, J.R. Frade, J. Mater. Sci. 36 (2001) 1105.
[37] E. Jud, L.J. Gauckler, J. Electroceram. 15 (2005) 159.
[38] J.E. Fallah, L. Hilaire, M. Romeo, F.L. Normand, J. Electron Spectrosc. Relat. Phenom. 73 (1995) 89.
[39] M.V. Rama Rao, T. Shripathi, J. Electron Spectrosc. Relat. Phenom. 87 (1997) 121.
[40] G.A. Carson, M.H. Nassir, M.A. Langel, J. Vac. Sci. Technol. A 14 (1996) 1637.
[41] P. Datta, P. Majewski, F. Aldinger, Mater. Charact. 60 (2009) 138.
[42] S.C. Petitto, M.A. Langell, J. Vac. Sci. Technol. A 22 (2004) 1690.
[43] J.L. Gautier, E. Rios, M. Gracia, J.F. Marco, J.R. Gancedo, Thin Solid Films 311 (1997) 51.
[44] J.D. Nicholas, L.C.D. Jonghe, Solid State Ionics 178 (2007) 1187.
[45] E. Barsoukov, J.R. Macdonald, Impedance Spectroscopy: Theory, Experiment, and Applications, John Wiley & Sons, Inc., 2005, 246 p.
[46] V. Gil, J. Tartaj, C. Moure, P. Durán, J. Eur. Ceram. Soc. 26 (2006) 3161.
[47] S. Banerjee, P.S. Devi, D. Topwal, S. Mandal, K. Menon, Adv. Funct. Mater. 17 (2007) 2847.
[48] M.-F. Han, S. Zhou, Z. Liu, Z. Lei, Z.-C. Kang, Solid State Ionics 192 (2011) 181.
[49] J.A. Dean, Lange's Handbook of Chemistry, McGraw-Hill, 1999.
[50] H. Yamamura, K. Matsui, K. Kakinuma, T. Mori, Solid State Ionics 123 (1999) 279.
[51] D. Pérez-Coll, P. Núñez, J.R. Frade, J. Electrochem. Soc. 153 (2006) A478.